



## Evaluation on La<sub>2</sub>O<sub>3</sub> garlanded ceria heterostructured binary metal oxide nanoplates for UV/ visible light induced removal of organic dye from urban wastewater

C. Maria Magdalane<sup>a,b</sup>, K. Kaviyarasu<sup>c,d,\*</sup>, N. Matinise<sup>c,d</sup>, N. Mayedwa<sup>c,d</sup>, N. Mongwaketsi<sup>c,d</sup>, Douglas Letsholathebe<sup>e</sup>, G.T. Mola<sup>f</sup>, Naif Abdullah Al-Dhabi<sup>g</sup>, Mariadhas Valan Arasu<sup>g</sup>, M. Henini<sup>c,h</sup>, J. Kennedy<sup>c,i</sup>, M. Maaza<sup>c,d</sup>, B. Jeyaraj<sup>b</sup>

<sup>a</sup> Department of Chemistry, St. Xavier's College (Autonomous), Tirunelveli, 627002, India

<sup>b</sup> LIFE, Department of Chemistry, Loyola College (Autonomous), Chennai, 600034, India

<sup>c</sup> UNESCO-UNISA Africa Chair in Nanosciences/Nanotechnology Laboratories, College of Graduate Studies, University of South Africa (UNISA), Muckleneuk Ridge, P O Box 392, Pretoria, South Africa

<sup>d</sup> Nanosciences African Network (NANOAFNET), Materials Research Department (MRD), iThemba LABS-National Research Foundation (NRF), 1 Old Faure Road, 7129, P O Box 722, Somerset West, Western Cape Province, South Africa

<sup>e</sup> Department of Physics, University of Botswana, Private Bag 0022, Gaborone, Botswana

<sup>f</sup> School of Chemistry Physics, University of KwaZulu-Natal, Pietermaritzburg Campus, Private Bag X01, Scottsville, 3209, South Africa

<sup>g</sup> Addiriyah Chair for Environmental Studies, Department of Botany and Microbiology, College of Science, King Saud University, P.O. Box 2455, Riyadh 11451, Saudi Arabia

<sup>h</sup> School of Physics and Astronomy, Nottingham Nanotechnology and Nanoscience Centre, University of Nottingham, Nottingham, NG7 2RD, United Kingdom

<sup>i</sup> National Isotope Centre, GNS Science, Lower Hutt, 5010, New Zealand

### ARTICLE INFO

#### Keywords:

CeO<sub>2</sub>:La<sub>2</sub>O<sub>3</sub>  
Heterogeneous catalysts  
Electron microscopy  
Photocatalytic activity  
RhB dye

### ABSTRACT

A low energy bandgap between Ce<sup>3+</sup> and Ce<sup>4+</sup> states in cerium oxides, high oxygen mobility and high oxygen storage capacity are the properties that qualify them to be the most widely used heterogeneous catalysts. This present work is an account of studies that were carried out on the synthesis and catalytic properties of pure CeO<sub>2</sub>, CeO<sub>2</sub>/La<sub>2</sub>O<sub>3</sub> based binary metal oxide nanostructures prepared by the hydrothermal method. Our results revealed that the synthesis temperature and pressure during hydrothermal reactions played a critical role in controlling the shape, size, oxygen vacancy, and low temperature reducibility in CeO<sub>2</sub> based nanostructures. In addition, OH<sup>-</sup> ion concentration was found to play an important role in engineering the lattice constants and oxygen vacancy defects. The present report demonstrated that the hydrothermal synthesis is a facile one step approach for the preparation of compositionally homogeneous cerium based binary metal oxide nanostructures, in which CeO<sub>2</sub>/La<sub>2</sub>O<sub>3</sub> mixed oxides have a superior low-temperature oxygen release capability compared to pure CeO<sub>2</sub>. We have also demonstrated that the nanomaterials are proved to have higher catalytic performance at low temperatures as compared to pure ceria nanoparticles.

### 1. Introduction

Photon-induced catalysts are used efficiently in waste water refinement to remove the highly carcinogenic and poisonous organic waste materials, such as deadly organic synthetic dyes, herbicides and pesticides, which are involved in different fields. Semiconductor photocatalysts induced by UV and visible light have been carried out widely to interpret the cleaning of polluted water, creation of renewable hydrogen energy source from water splitting, and the discharge of

pernicious microorganisms (Zhao et al., 1998). Titanium dioxide is the most generally used photocatalysts owing to its non-toxicity, minimum cost, stability and powerful oxidizing property the bandgap of TiO<sub>2</sub> is 3.2 eV; it can consume about 4% of UV light energy, which leads to less efficiency in huge scale industrial applications (Yin et al., 2012). There are many problems in our environment to work out solutions and it is important and hypercritical to widen a cost-effective, sustainable and steady photocatalyst that is focused by light resource, which can account for about 45% of light energy. Over the last few years, substantial

\* Corresponding author. UNESCO-UNISA Africa Chair in Nanosciences/Nanotechnology Laboratories, College of Graduate Studies, University of South Africa (UNISA), Muckleneuk Ridge, P O Box 392, Pretoria, South Africa.

E-mail addresses: [kavi@tlabs.ac.za](mailto:kavi@tlabs.ac.za), [k.kaviyarasu@outlook.com](mailto:k.kaviyarasu@outlook.com) (K. Kaviyarasu).

<https://doi.org/10.1016/j.sajce.2018.09.003>

Received 16 July 2018; Received in revised form 28 August 2018; Accepted 17 September 2018

1026-9185/ © 2018 The Author. Published by Elsevier B.V. on behalf of Institution of Chemical Engineers. This is an open access article under the CC BY-NC-ND license (<http://creativecommons.org/licenses/by-nc-nd/4.0/>).

efforts have been made towards the enlargement of extremely effective and study of photocatalysts for the oxidative decomposition of organic dyes to undistruptive end-products, such as carbon dioxide (CO<sub>2</sub>), and water (H<sub>2</sub>O). The oxides of metal like Y<sub>2</sub>O<sub>3</sub>, WO<sub>3</sub>, CeO<sub>2</sub>, and SnO<sub>2</sub> and their composites have been reported to have better electronic properties with exceptional reusability owing to their extensive surface area with improved photocatalytic performance (Kennedy et al., 2011; Kaviyarasu et al., 2017b). Specifically, nano sized rare earth metal oxides (REMO) like CeO<sub>2</sub>, and La<sub>2</sub>O<sub>3</sub> are more and more used in a variety of latest technologies like the invention of fibres optics, sensors and catalytic filter-neutralizers of exhaust gases of cars, phosphors, lasers and superconductors (Nasir et al., 2014). Among all the rare-earth metal oxides, only ceria-based nanostructures have generated great interest as a practical way to hike the efficiency of various photocatalytic and photocapacitive applications.

Ceria (CeO<sub>2</sub>) NPs is an affirmative photocatalyst and super capacitor substance since it is a most available and cheap inner transition metal oxide with outstanding redox properties. Furthermore, the platelet morphology of nanomaterials with a superior active surface area has an outstanding outcome on the catalytic field (Bakkiyaraj et al., 2016). The wide bandgap of ceria semiconductor is 3.2 eV, which restricts its use as an electronic material and as a photocatalyst. Co-catalyst with ceria is a superior technique for the alteration of the band structure and to increase the defects for example oxygen positions in CeO<sub>2</sub>, which play a vital role in its photocatalytic performance (Jaoude et al., 2016). The inter conversion of Ce<sup>4+</sup> to Ce<sup>3+</sup> ratio enhances the photon-induced dye degradation by narrowing the bandgap of CeO<sub>2</sub>. Muduli et al., discussed the mesoporous cerium oxide nanospheres and its visible-light driven photocatalytic degradation of dyes (Muduli et al., 2014). Zhang et al., synthesized CeO<sub>2</sub> hierarchical nanorods and nanowires by electrochemical method with excellent photocatalytic activities (Zhang et al., 2014). Lin et al., investigated the application of 1-D Cerium Oxide nanomaterials (Lin and Chowdhury, 2010). Hemalatha et al., synthesized the polyvinyl alcohol-cerium oxide nanocomposite films (Hemalatha and Rukmani Synthesis, 2016). Gu et al., synthesized CeO<sub>2</sub> nanoparticles sensitized CdS nanorods as a photocatalyst using visible-light for the photocatalytic degradation of Rhodamine-B (Gu et al., 2015). Zhu et al., proved the superior photocatalytic activity of Ce-doped Zn-Al multi-metal oxide composites in which ceria increases the generation of excitons (Zhu et al., 2016). Lv et al., synthesized CeO<sub>2</sub>/ZnO composite oxide with improved photocatalytic activity due the synergic effect of ceria (Lv et al., 2016). Ceria in addition increases the oxygen vacancy in the composite. However, the preparations of lanthanum incorporated by ceria nanoplates and its mechanism have not been reported so far. CeO<sub>2</sub> based materials show excellent electrical mobility, tremendous specific active surface area, higher thermal conductivity and outstanding mechanical properties. Hence, it is applied widely as a remarkable support and electron transport material. Specifically, the addition of inner transition metal oxide (ITMO) enhances the strain inside the lattice and stimulates a creation of crystal defect in the ceria matrix, which can convert the material to a good semiconductor. Lanthanum oxide (La<sub>2</sub>O<sub>3</sub>) belongs to rare earth oxides series and exhibits extraordinary property, which is a potential material in various fields and can be easily doped with cerium. Both the metal oxides have a cubic crystal structure with very comparable lattice constants and trivalent environment with almost the same ionic radius. Therefore, to the best of our knowledge, there has been no investigation on the photodegradation of organic synthetic dye effluent studies by using CeO<sub>2</sub>/La<sub>2</sub>O<sub>3</sub> nanostructures with high performance (Ahmed, 2015).

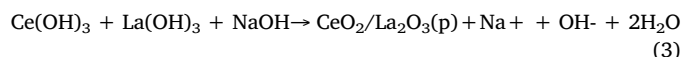
In this current investigation, an effortless and scalable synthesis method was developed for the preparation of CeO<sub>2</sub>/La<sub>2</sub>O<sub>3</sub> nanostructures in different ratios through a facile and efficient hydrothermal method, which provides uniform La<sub>2</sub>O<sub>3</sub> anchored on CeO<sub>2</sub> nanoplates (Faisal et al., 2013). The hydrothermal method has many advantages like high purity and efficiency of the sample, which has a

major role in controlling active surface area, grain size and shape of nanomaterials. Thus, in our present investigation, we have chosen hydrothermal method, for the synthesis of hierarchical (La<sub>2</sub>O<sub>3</sub>) lanthanum oxide decorated ceria (CeO<sub>2</sub>) nanoplates and this study involves the investigation of the optical and structural properties as well as the photocatalytic degradation ability of the CeO<sub>2</sub>/La<sub>2</sub>O<sub>3</sub> nanostructures using the organic model pollutant dye. These can upgrade the advance modification of CeO<sub>2</sub>/La<sub>2</sub>O<sub>3</sub> nanostructures based devices for forthcoming energy or environment-related applications. On illumination of visible light, the catalyst was found to produce reactive oxygen species (ROS), which might account for the decay of dyes into small fractions.

## 2. Experimental methods

### 2.1. Materials and methods

All the chemicals utilised in this experiment were of analytically pure grade and used without further purification. Cerium nitrate and lanthanum nitrate in 1:0, 1:1, 2:1, 1:2 and 0:1 M ratios solution were prepared by using double deionised water and the required amount of sodium hydroxide was added to the mixture solution and treated via hydrothermal route to synthesize pure and CeO<sub>2</sub>/La<sub>2</sub>O<sub>3</sub> binary metal oxides in 1:1, 2:1 and 1:2 M ratios, which were labelled as CeO<sub>2</sub>, La<sub>2</sub>O<sub>3</sub> Ce<sub>1</sub>/M<sub>1</sub>, Ce<sub>2</sub>/M<sub>1</sub> and Ce<sub>1</sub>/M<sub>2</sub> respectively. Cerium nitrate and lanthanum nitrate salts of (0.1 M) were dissolved in distilled water with vigorous stirring, mixed together with constant stirring for 1 h and 0.5 M NaOH was added drop wise until the pH has reached about ~10.5. The pH value of the solution was recorded using a digital pH meter. The mixture was transferred into stainless steel autoclave which was sealed tightly; it was kept in an air oven heated at 150 °C for 12 h. The formed pale-yellow precipitate was filtered, washed with double distilled water followed by ethyl alcohol and dried in an oven at 80 °C under air atmosphere. The growth mechanism of CeO<sub>2</sub>/La<sub>2</sub>O<sub>3</sub> nanomaterials is explained based on simple chemical reactions and nucleation given below.



### 2.2. Characterization of catalyst materials

The crystalline structure and phases of pure and CeO<sub>2</sub>/La<sub>2</sub>O<sub>3</sub> heterostructured binary metal oxide nanostructures were examined on a Siemens D-500 diffractometer using Ni-filtered Cu-K<sub>α</sub> radiation at λ = 1.540 Å in the 2θ ranges from 20° – 70° with a scan speed of 2° per minute via Bragg-Brantano configuration. Fourier transform infrared spectrometer (FTIR) (Excalibur Series FTIR) was used to identify the functional groups in the synthesized samples. The morphological structure of the synthesized nanostructures was done by Scanning electron micrograph (SEM) (JEOL JSM-5300 microscope with acceleration voltage 15 kV). The optical property of samples was examined by using UV-Vis (DRS) Spectra of nanomaterials were recorded on a Shimadzu spectrophotometer (UV-2450) in the collection of 200 nm–800 nm range. The elemental nature of individual nanocrystals was determined by energy dispersive X-ray spectroscopy (EDX) analysis in scanning electron microscopy (SEM) mode with a focused electron probe. High resolution transmission electron microscopy (HRTEM) was used to establish the showing crystal facets in individual La<sub>2</sub>O<sub>3</sub> garlanded ceria heterostructured binary metal oxide nanostructures. Measurement of the emission spectra of pure and CeO<sub>2</sub>/La<sub>2</sub>O<sub>3</sub> heterostructured binary metal oxide nanostructures has been recorded using a Lab RAM HR (UV) spectrophotometer equipped with 325 nm laser

source with CCD detector.

### 2.3. Photocatalytic activity

The photocatalytic behaviour of CeO<sub>2</sub> based nanostructures was examined by studying the photocatalytic decomposition efficiency of dye. Degradation reactions were carried out with different pH at 3, 7 and 9 and the initial pH of the suspensions was adjusted by the addition of either NaOH or HCl solutions. The dye solutions were equilibrated with the catalyst for 1 h prior to UV irradiation. Time dependent degradation processes of dye molecules in the presence and absence of nanostructures and light are analysed through UV–Vis absorption spectroscopy. It is worth mentioning that the cationic RhB dye does not degrade under UV light irradiation without the addition of a photocatalyst. Photocatalytic degradation of dye was carried out in different ppm level under UV irradiation with 365 nm (30 W powers). Catalyst (0.030 g) was added to 100 ml of aqueous dye solution, and the solution was stirred in the dark for 30 min to attain absorption - desorption equilibrium between the catalyst and the dye. After 30 min of equilibrium, the samples were irradiated under the respective sources. After irradiation, the solution was centrifuged and filtered to remove the dispersed catalyst particles. At each given irradiation time interval, 2 ml of the test sample was taken and the concentration of dye in the solution was determined by using a UV–Visible spectrophotometer. The efficiency of degradation ( $\eta$ ) was calculated by equation (4). Similarly, the same experiment was carried out in visible light using metal halide lamp.

$$\eta = \frac{A_0 - A_t}{A_0} \times 100 \quad (4)$$

where  $A_0$  is the absorption maximum at time  $t$ , and  $A_t$  is the absorption maximum after complete degradation of dye solution.

## 3. Results & discussion

### 3.1. Crystalline structure and phase diffraction

The powder x-ray diffraction (PXRD) of the chemical precipitation assisted hydrothermal route synthesized CeO<sub>2</sub>, La<sub>2</sub>O<sub>3</sub> and CeO<sub>2</sub>/La<sub>2</sub>O<sub>3</sub> binary metal oxide in 1:1, 2:1 and 1:2 M ratios respectively are shown in Fig. 1. In the obtained diffraction pattern, each peak can be assigned to either CeO<sub>2</sub> or La<sub>2</sub>O<sub>3</sub> phase and shows that there are no other new phases like its corresponding hydroxide, metallic and other phase of metal oxide. This high purity ceria metal oxides reveal that the major peaks of CeO<sub>2</sub> has  $2\theta = 28.50^\circ, 33.12^\circ, 47.31^\circ, 56.18^\circ, 59.09^\circ, 69.51^\circ, 76.60^\circ$  and  $79.17^\circ$  corresponding to the (111), (200), (220), (311), (222), (400), (331) and (420) respectively with cubic phase. Fig. 1 represents the effect of La loading on the crystalline phases of the ceria nanomaterials. It is proved that the pure and ceria based composite has fluorite cubic structure as a main phase in all cases of prepared materials. La<sub>2</sub>O<sub>3</sub> has  $2\theta = 27.00^\circ, 33.19^\circ, 36.71^\circ, 44.78^\circ, 53.01^\circ, 55.51^\circ$  and  $72.0^\circ$  corresponding to the (222), (411), (332), (440), (622), (444) and (662) respectively with cubic phase. The cubic lattice remains the same in the presence of La<sup>3+</sup> ions and the diffraction phases of the La decorated binary ceria metal oxide nanostructure compared to the pure CeO<sub>2</sub>, a shift in the phases was observed in the direction of lower  $2\theta$  angles, due to the larger cation, La<sup>3+</sup> substituting for Ce<sup>4+</sup> in the CeO<sub>2</sub> lattice. In the observed diffraction pattern of the ceria rich nanostructures like Ce<sub>2</sub>/La<sub>1</sub> and Ce<sub>1</sub>/La<sub>1</sub> there is no additional diffraction peaks emerging. These may be corresponding to the presence of only cubic CeO<sub>2</sub> proving the absence of other phases in the prepared samples. Fig. 1 shows the diffraction phases of the Ce<sub>1</sub>/La<sub>2</sub> nanomaterials and it is evidently seen that there is a shift in the highest intensity peak at  $28^\circ$  related to the (111) reflection. The shifts in the peaks position indicate an enlargement in the CeO<sub>2</sub> cubic lattice. Furthermore, this could be a reason for devising CeO<sub>2</sub> matrix nanoplates becoming a

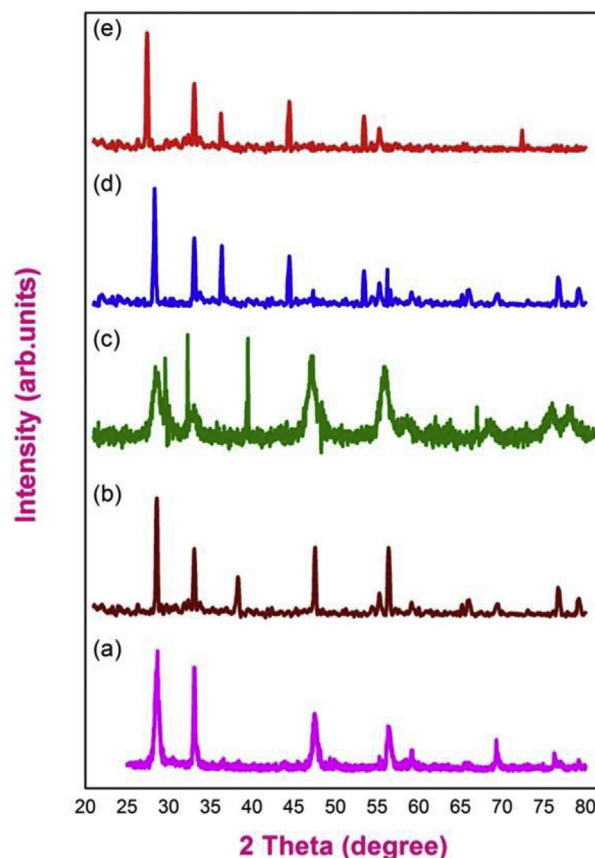


Fig. 1. X-ray diffraction pattern of synthesized CeO<sub>2</sub>/La<sub>2</sub>O<sub>3</sub> nanostructures (a) pure ceria (b) Ce<sub>1</sub>/La<sub>1</sub> (c) Ce<sub>2</sub>/La<sub>1</sub> (d) Ce<sub>1</sub>/La<sub>2</sub> and (e) pure La<sub>2</sub>O<sub>3</sub>.

better host material candidate for accommodating ionic dopants with a bigger size than Ce<sup>4+</sup> (e.g. La<sup>3+</sup> in the current study) with minimal disruption of the lattice (reducing the lattice stress). We assign the shift in the peak position the difference in ionic size between Ce<sup>4+</sup> and La<sup>3+</sup>. Since La<sup>3+</sup> has a larger ionic size compared to Ce<sup>4+</sup>, doping with La<sup>3+</sup> in CeO<sub>2</sub> lattice will result in expanded lattice. Every Ce<sup>4+</sup> is surrounded by eight O<sup>2-</sup> and every La<sup>3+</sup> is surrounded by seven O<sup>2-</sup> (Korake et al., 2014).

### 3.2. Fourier transform infrared spectroscopy (FTIR) analysis

The main functional groups in the pure ceria and cerium oxide/lanthanum oxide (1:1, 1:2 and 2:1 M ratios) binary metal oxide heterostructured nanomaterials were analysed by FTIR spectra and are presented in Fig. 2. The absorption band near 3483 cm<sup>-1</sup> is mainly due to the OH stretching frequency of MO (OH) phase. Also, it is proved that the synthesized sample is a mixed composite of cerium/lanthanum oxide (Saravanakumar et al., 2018). The lattice vibration modes of M-O and O-M-O (Ce, La) were observed in the low frequency region 400 cm<sup>-1</sup> - 1400 cm<sup>-1</sup>. An absorption broad band is observed around 510 cm<sup>-1</sup> for pure ceria, which is corresponding to M-O bond (Iavkova et al., 2015). For the cerium oxide/lanthanum oxide (Ce<sub>1</sub>/Y<sub>1</sub> and Ce<sub>2</sub>/La<sub>1</sub> ratios) binary metal oxide heterostructured nanomaterials the absorption broad band occurs at 480 cm<sup>-1</sup>, whereas Ce<sub>1</sub>/La<sub>2</sub> molar ratio sample shows the band at 560 cm<sup>-1</sup> due to the higher amount of lanthanum oxide. The band near 1530 cm<sup>-1</sup> is assigned to the bending vibration of water molecules.

### 3.3. High resolution scanning electron microscopy (HRSEM) analysis

The surface morphology and detailed size of the pure CeO<sub>2</sub> and

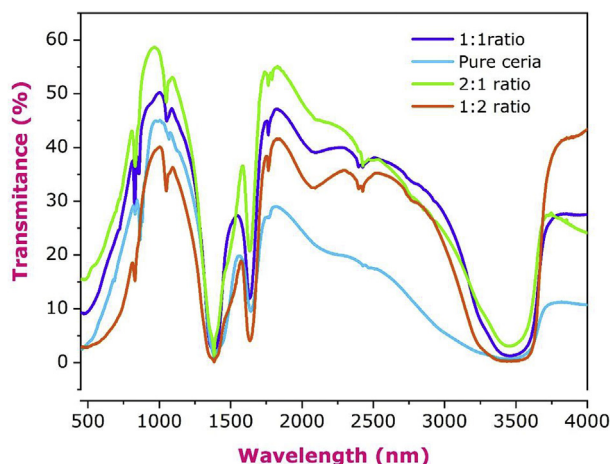


Fig. 2. FTIR spectra of  $\text{CeO}_2/\text{La}_2\text{O}_3$  nanostructures (a)  $\text{Ce}_1/\text{La}_1$  (b)  $\text{Ce}_2/\text{La}_1$  and (c)  $\text{Ce}_1/\text{La}_2$ .

$\text{CeO}_2/\text{La}_2\text{O}_3$  binary metal oxide nanostructures synthesized by the hydrothermal method were visualised by HRSEM. Fig. 3(a–h) shows the HRSEM images of pure  $\text{CeO}_2$  and  $\text{CeO}_2/\text{La}_2\text{O}_3$  in different ratio like 1:1, 2:1 and 1:2 respectively. Fig. 3(a and b) shows the formation of non-uniform shapes of  $\text{CeO}_2$  nanostructures with high agglomeration in the particle size range from 85 to 50 nm. The SEM images of  $\text{Ce}_2/\text{La}_1$  nanostructure Fig. 3(g and h) at low and high magnification suggest that the morphology of the heterostructured clusters composites is ceria bed with platelet shape. It demonstrates clearly that the change in the morphology of the nanostructures with the incorporation of rare earth metal oxide  $\text{La}^{3+}$ . This entire synthesized sample results with a smaller grain size consisting of main (10 nm - 40 nm) subunits with less porosity. Nucleation and growth frequency increases with increase in amount of La, thus agglomeration is more in the  $\text{Ce}_1/\text{La}_2$  sample as shown in Fig. 3(f). In the present work, it seems that the aggregation is the leading mechanism which happened during the crystallization of gel-network foremost to macroscopic particles. The particles are uniformly distributed and attached to each other through the grain boundary to form agglomerated particles. Cerium oxide/lanthanum oxide  $\text{Ce}_1/\text{La}_1$  shows that the porous cerium oxide is a platelet shaped in which lanthanum oxide embedded with less grains size. When lanthanum oxide is doped into the cerium oxide, the morphology was found to change. Fig. 3(g) shows the high magnification of the sample with the spherical shaped lanthanum oxide particles dispersed in the cerium oxide bed clusters and it is clearly seen that small particle dispersed on the surface of the platelet like structure. The average particle size was estimated and it is between 10 nm and 40 nm. HRSEM image

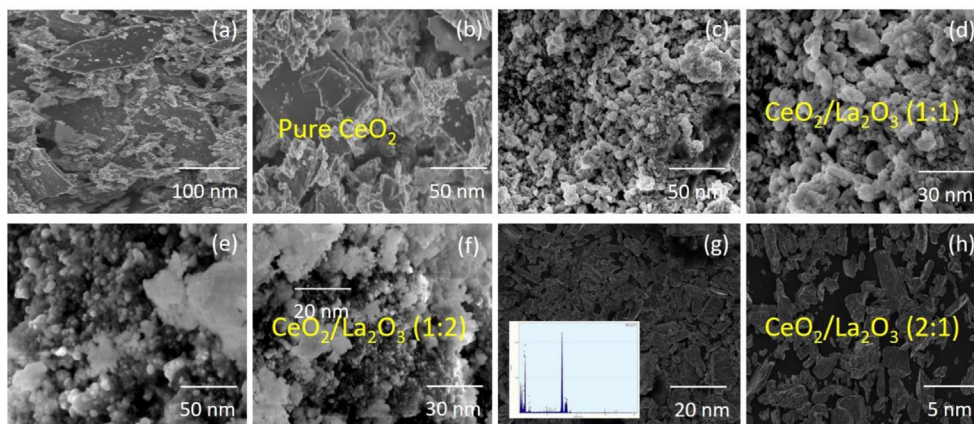


Fig. 3. HRSEM morphology evolution of  $\text{CeO}_2/\text{La}_2\text{O}_3$  nanostructures (a, b) Pure  $\text{CeO}_2$ , (c, d)  $\text{Ce}_1/\text{La}_1$ , (e, f)  $\text{Ce}_1/\text{La}_2$  and (g, h)  $\text{Ce}_2/\text{La}_1$ .

of the  $\text{Ce}_2/\text{La}_1$  nanostructure clearly shows that there is no aggregation and agglomeration of plates which suggests that the lanthanum oxide particles were well dispersed in the platelet shaped ceria matrix shown in Fig. 3(h). It is confirmed that the lanthanum atoms were well and consistently dispersed in the cerium matrix. From the EDX spectrum respective elements of the synthesized sample were identified and the elemental compositions are cerium (Ce), lanthanum (La) and oxygen (O). Carbon tape was utilised to fix the synthesized sample in the analysis, which gave a signal for carbon in the EDX spectrum. Inset of Fig. 3(g) shows an EDX spectrum for the sample prepared by hydrothermal method and the metal oxides are dispersed at microscopic level.

### 3.4. High resolution transmission electron microscopy (HRTEM)

The microstructure nature of the prepared pure and  $\text{CeO}_2/\text{La}_2\text{O}_3$  binary metal oxide nanostructures were further investigated by HRTEM. Fig. 4(a–p) shows the typical HRTEM images of pure  $\text{CeO}_2$  and  $\text{CeO}_2/\text{La}_2\text{O}_3$  in different ratios (1:1, 1:2 and 2:1). Pure  $\text{CeO}_2$  shows the presence of irregular mixed morphology with sizes in the range of 100–80 nm as shown in Fig. 4(a–d), whereas  $\text{Ce}_1/\text{La}_1$  binary metal oxides nanostructure as shown in Fig. 4(e–h) shows semi spherical as well as plate like morphology with sizes in the range of 50–20 nm spread with smaller particles of the other metal oxides.  $\text{Ce}_1/\text{La}_2$  sample consists of irregular shape with higher agglomeration shown in Fig. 4(m–p). As displayed, the metal oxide exhibited platelet like morphology with less agglomeration and particles were evenly distributed in between them. HRTEM image of  $\text{CeO}_2/\text{La}_2\text{O}_3$  ( $\text{Ce}_2/\text{La}_1$ ) nanostructures at low and high magnification is illustrated in Fig. 4(i–l), and it proves that the  $\text{La}^{3+}$  nanostructures are anchored in between the surface of  $\text{CeO}_2$  nanostructures with a particle size of 10–30 nm. Selected Area Electron Diffraction (SAED) confirms the high crystalline nature of the nanocubes. Exactly, lattice planes related with cubic  $\text{CeO}_2$  with SAED is shown in Fig. 4; HRTEM images demonstrate the lattice fringes due to single crystalline planes as clearly observed.

### 3.5. Diffuse reflectance spectral (DRS) studies

The optical property was examined for the synthesized sample by UV-Visible diffuse reflectance spectroscopy. The amount of ceria influences the absorption property of the materials with red shift. An insignificant shift in the peak absorption wavelength was observed for the prepared nanomaterials, which might be due to the formation of high crystalline phases of ceria. Calculation of the bandgap ( $E_g$ ) was carried out by fitting the UV-Visible absorption data with the direct transition equation by extrapolating of the linear portions of the curves to absorption equal to zero. The bandgap was calculated from Tauc

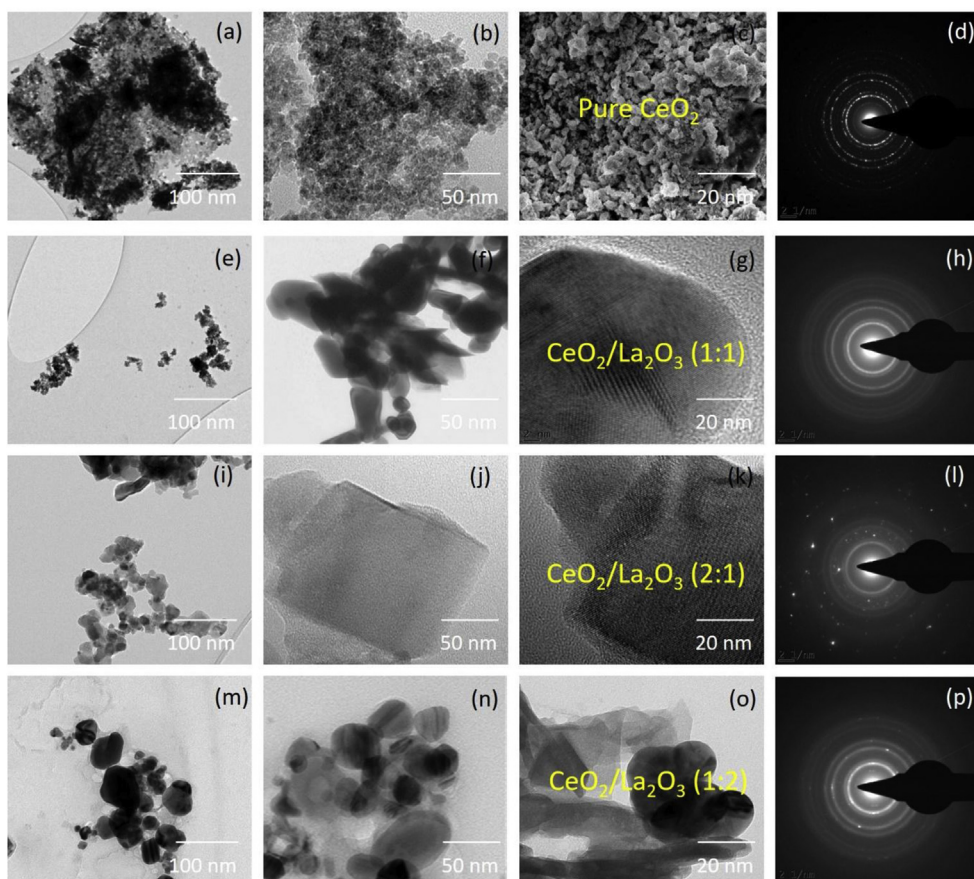


Fig. 4. HRTEM images of  $\text{CeO}_2/\text{La}_2\text{O}_3$  nanostructures (a–d) Pure  $\text{CeO}_2$ , (e–h)  $\text{Ce}_1/\text{La}_1$ , (i–l)  $\text{Ce}_2/\text{La}_1$  and (m, p)  $\text{Ce}_1/\text{La}_2$ .

relation for all synthesized samples as shown in Fig. 5(a and b). The reflectance (R) was rehabilitated into corresponding absorption coefficient with the help of Kubelka-Munk function is given in below Eq. (5),

$$F(R) = \alpha \cdot (1 - R^2) / 2R \quad (5)$$

Where  $F(R)$  is Kubelka-Munk function,  $\alpha$  is the absorption coefficient. R is the reflectance. Therefore, the Tauc relation is given by Eq. (6),

$$(F(R)h\nu) = A (h\nu - E_g)^n \quad (6)$$

Where  $n = 1/2$  represents indirect transition, which gives rise to indirect bandgap and  $n = 2$  is the direct bandgap. In diffuse reflectance absorption spectra, a graph is drawn in between  $(F(R)h\nu)^{1/2}$  vs photon energy gives indirect bandgap and  $(F(R)h\nu)^2$  versus photon energy suggesting a direct bandgap transition. The calculated bandgap values of the synthesized  $\text{CeO}_2$ ,  $\text{Ce}_1/\text{La}_1$ ,  $\text{Ce}_1/\text{La}_2$ ,  $\text{Ce}_2/\text{La}_1$  and  $\text{La}_2\text{O}_3$  samples were found to be 3.21, 3.17, 3.05, 2.98 and 3.18 eV respectively. The observed results evidently signify that there is drop in the bandgap values with a grain size for the prepared nanostructures, which is due to the quantum confinement effects. The direct bandgap energies are generally found to increase with the particle size and morphology of the nanostructures, when compared to the individual cerium oxide. The changes in the bandgap energy are due to the preparation conditions, grain size, shape and structural changes in the lattice (Saravanakumar et al., 2018). Thus, the nanocrystal size decreases with increase in the effective width of the forbidden band. Ceria particles in nanolevel displayed high opaqueness in the UV region and high transparency in the visible region. This may be due to the charge transition from  $2p$  orbital of oxygen to  $4f$  orbital of cerium in  $\text{O}^{2-}$  and  $\text{Ce}^{4+}$  of cubic phase of ceria. The amount of lanthanum content increase leads to changes in the optical bandgap of ceria. This may be due to the changes in the structural defects or oxygen vacancies in the crystal structure in the

synthesized samples (Srinivasan et al., 2010). It is known that when the effective width of the forbidden bandgap is increased, there will be a decrease in the size.

### 3.6. $\mu$ -Raman spectroscopy

The structural elucidation of pure ceria and  $\text{CeO}_2/\text{La}_2\text{O}_3$  (2:1) binary metal oxide nanoplates are examined by Raman spectroscopy as shown in Fig. 6(a and b), which is a promising technique for the identification of defects level in the nanostructures. It is mainly used to categorise the dissimilar structures, because it directly investigates the structures and bonds by its vibrational spectrum. Pure  $\text{CeO}_2$  nanostructures exhibit a broad band at  $458 \text{ cm}^{-1}$  which generally corresponds to the  $F_{2g}$  Raman active-mode of cubic fluorite structure. Thus, the broad and highly intense band at  $458 \text{ cm}^{-1}$  in the prepared nanostructures proves the grown ceria is in well-arranged crystal form of fluorite cubic phase of ceria, whereas in the case of  $\text{CeO}_2/\text{La}_2\text{O}_3$  (2:1) binary metal oxide nanoplates, the larger  $\text{La}^{3+}$  cation incorporated into the lattice of cerium atom leads to shift in the Raman peak at a higher wavenumber. This is due to the changes in the cell parameter of the ceria system. The bonding in the lanthanum oxide is longer than the ceria. Hence, there is a slight distortion in the cubic fluorite lattice of the ceria. This lattice distortion caused changes in the  $F_{2g}$  Raman shift (Zhao et al., 2015a).

### 3.7. Photoluminescence studies

To examine the photogenerated excitons at room temperature, photoluminescence (PL) of pure cerium oxide and  $\text{CeO}_2/\text{La}_2\text{O}_3$  (1:1, 2:1, 1:2) binary metal oxide nanostructures were examined in between the range of 300–600 nm, as shown in Fig. 7(a–d), with an excitation

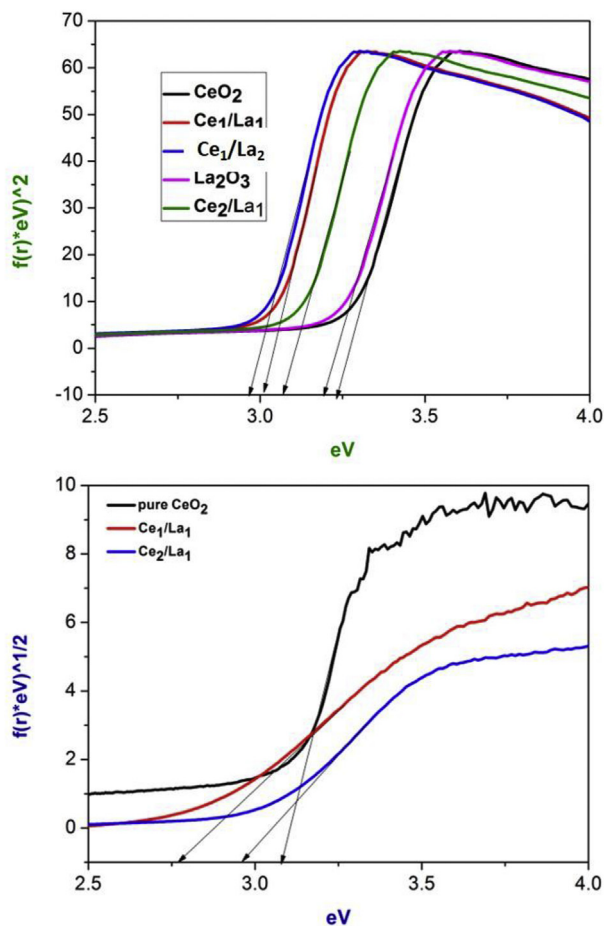


Fig. 5. DRS spectra (a) direct bandgap for pure  $\text{CeO}_2$ , pure  $\text{La}_2\text{O}_3$ ,  $\text{Ce}_1/\text{La}_1$ ,  $\text{Ce}_1/\text{La}_2$  and  $\text{Ce}_2/\text{La}_1$  (b) indirect bandgap of pure  $\text{CeO}_2$ ,  $\text{Ce}_1/\text{La}_1$  and  $\text{Ce}_2/\text{La}_1$  nanostructures.

wavelength of 355 nm. The PL spectra bands of pure ceria were observed at 320 nm and 360 nm corresponding to near band edge (NBE) emission in the UV region which is due to excitonic recombination. Fig. 7(b and c) shows the PL spectra of  $\text{CeO}_2/\text{La}_2\text{O}_3$  (1:1, 2:1) binary metal oxide nanostructures. Excitation at 355 nm exhibited emissions peaking at nearly at 410, 490, 520 and 565 nm. The strong blue emission was observed in the range of 400–490 nm and green band were observed at 520 and 565 nm. A blue emission band was detected at 415 nm for the  $\text{Ce}_1/\text{La}_2$  sample shown in Fig. 7(d). The bands detected at 390–570 nm are ascribed to the different stages of  $4f$  orbital of cerium and  $2p$  orbital of oxygen. The weak emission at 466 nm is associated to the abundant defects like disorder, which are connected to fast oxygen moving. The defect energy levels between Ce  $4f$  and O  $2p$  were originated to be exaggerated by the doping and compactness of imperfections in the crystals. The 2:1 sample displays the strong and broad emission bands in the blue-visible region that is due to the well-defined crystalline nature of the sample.

### 3.8. Photocatalytic activity

Photocatalytic activity of the binary metal oxides was evaluated by taking RhB as the model pollutant and the degradation studies were carried out at both UV light (365 nm) and visible light irradiation. The process conditions were optimized in terms of the following reaction variables. (a) Effect of irradiation time on the photodegradation of RhB (b) Effect of pH on the photodegradation of RhB (c) Effect of initial concentration of RhB (d) Effect of catalyst dose (e) Reusability of catalysts (f) Effect of catalyst on industrial waste water.

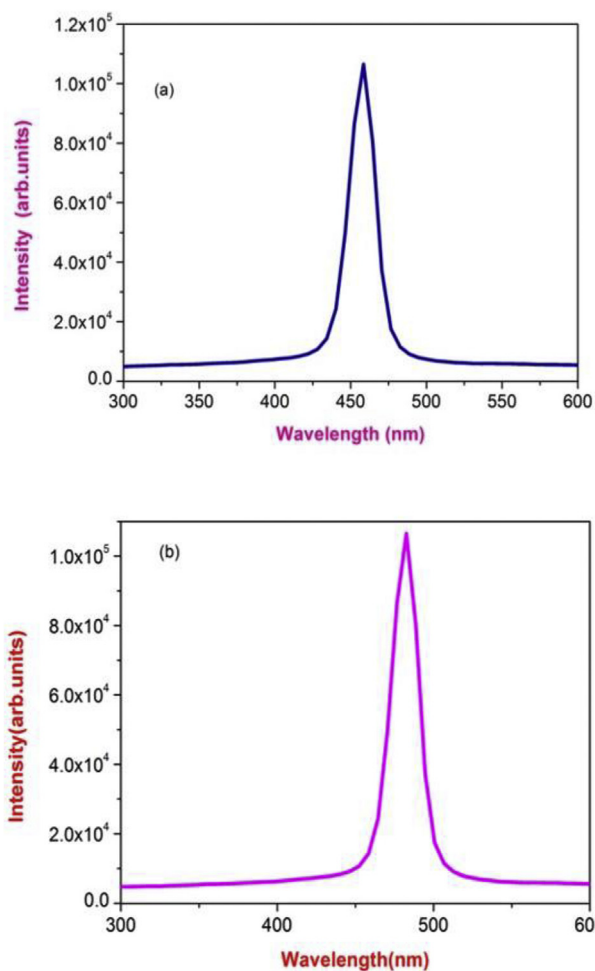


Fig. 6.  $\mu$ -Raman spectrum of  $\text{CeO}_2/\text{La}_2\text{O}_3$  nanostructures (a) pure ceria (b)  $\text{Ce}_2/\text{La}_1$ .

#### 3.8.1. Degradation of Rhodamine-B using $\text{CeO}_2/\text{La}_2\text{O}_3$ heterogeneous catalyst

The textile effluent Rhodamine-B is chosen as a pollutant due to its high stability to investigate its decomposition nature by the prepared nanosamples using UV light irradiation Fig. 8(a–c). The degradation capacity of all the samples with different ratios 1:0, 1:1, 1:2, 2:1 and 0:1 was investigated and recorded the absorption vs time (t) in min under UV/Visible light irradiation. The ratios between  $C_t$  (concentration of dye at different time intervals of UV exposure) and  $C_0$  (initial concentration) of the dye ( $C_t/C_0$ ), were plotted against the time of UV exposure, to compare the efficiency of the degradation under different conditions. The photocatalytic degradation efficiency of the different ratios samples shows the following order 1:1 = 2:1 > 1:2 > 1:0 = 0:1. It is observed that the  $\text{Ce}_1/\text{La}_1$  and  $\text{Ce}_2/\text{La}_1$  samples exhibit the best photocatalytic activity when compared with all other samples, due to their better specific surface area, more reactive sites, mesoporous, higher ability towards absorption of light, smaller in size with high dispersion usually leading to better photodegradation efficiently.

#### 3.8.2. Photocatalytic degradation of Rhodamine-B dye using $\text{CeO}_2/\text{La}_2\text{O}_3$ heterogeneous catalyst $\text{Ce}_2/\text{La}_1$ ratio

The photocatalytic decomposition activity of  $\text{CeO}_2/\text{La}_2\text{O}_3$  binary metal oxide nanoplates ( $\text{Ce}_2/\text{La}_1$ ) on RhB dye was carried out in the aqueous dispersions under UV light at room temperature. Various ceria based nanomaterials examined as photocatalyst in the literature which is given in Table 1. Degradation of RhB dye was not discussed anywhere

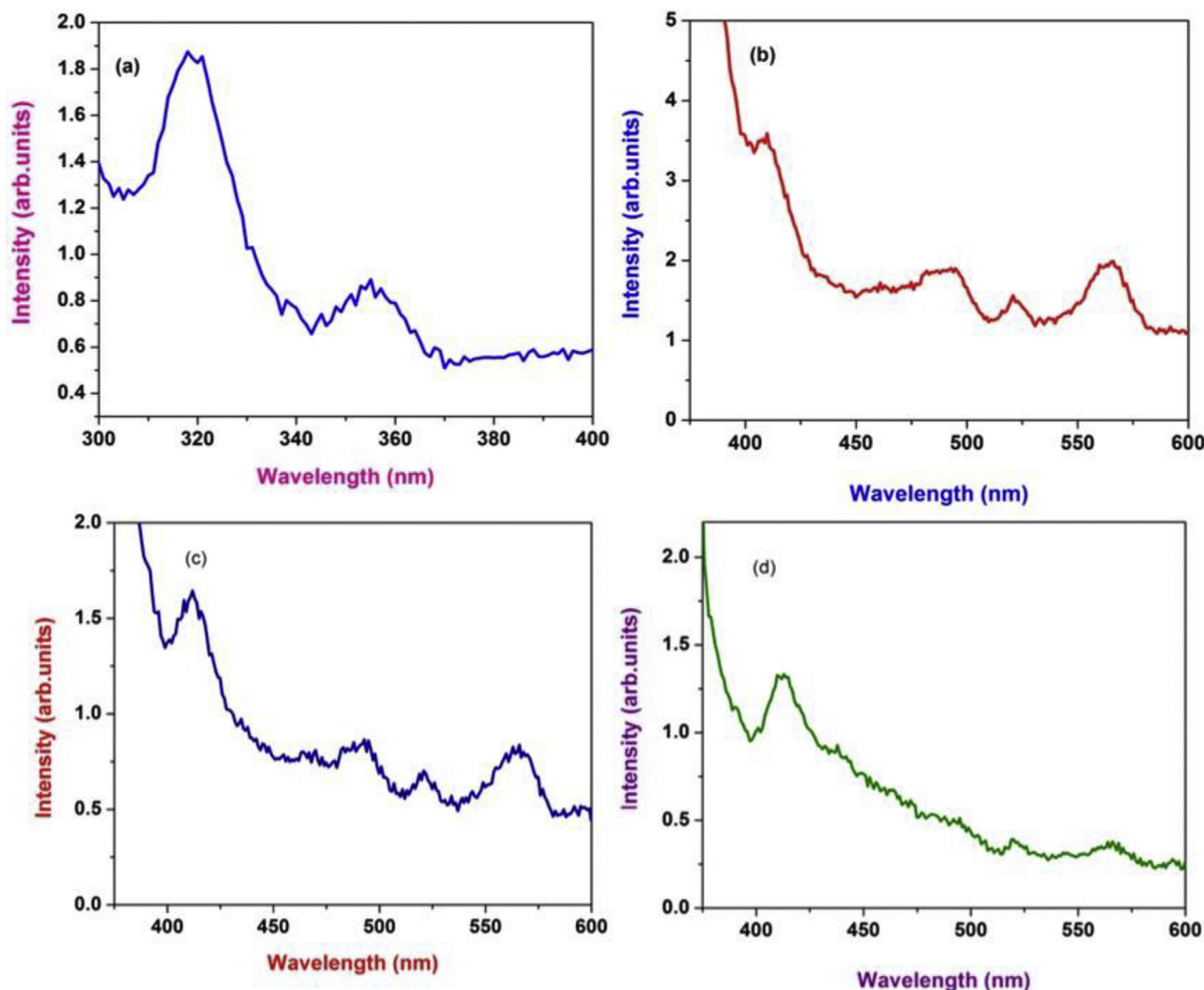


Fig. 7. Photoluminescence spectra of  $\text{CeO}_2/\text{La}_2\text{O}_3$  nanostructures (a) pure  $\text{CeO}_2$  (b)  $\text{Ce}_1/\text{La}_1$  (c)  $\text{Ce}_2/\text{La}_1$  and (d)  $\text{Ce}_1/\text{La}_2$ .

by our synthesized ceria based materials at various conditions. The photodecomposition process was carried out in reactor compartment consists of cylindrical borosilicate tubes. The aqueous Rhodamine-B solution (100 ml) containing 50 mg catalyst was mixed well for 30 min before the photo irradiation and the solution mixture was kept in the absence of light to reach the adsorption/desorption equilibrium among the catalyst and RhB molecules and thus the loss of organic synthetic dye molecules due to the adsorption can be considered. The mixture solution was then placed inside the reactor with addition of 5 ml of 20%  $\text{H}_2\text{O}_2$ . The suspension was purged with oxygen bubbling all the way through the experimentation with illumination of UV light. The samples (nearly 2.0 ml) at standard intervals throughout the irradiation process (30 min) with RhB dye solution were separated from the mixture by centrifugation before measurement of UV analysis. The decomposition process was confirmed by measuring the absorbance using UV-Visible spectrophotometer (UV- 2960) and the absorbance of RhB (10 ppm) was followed at 365 nm wavelength. All the prepared dye solutions were made and prepared with deionised water (Lv et al., 2016; Zhao et al., 2015a). The absorbance spectra of RhB are shown in Fig. 10(a–e). RhB dye adsorbed on the photocatalyst undergoes degradation mainly on the mixed  $\text{CeO}_2/\text{La}_2\text{O}_3$  binary metal oxide nanoplates. The amount of decomposition of the RhB dye was examined by monitoring its strength with and without  $\text{CeO}_2/\text{La}_2\text{O}_3$  binary metal oxide nanoplates after the attainment of the degradation. Fig. 8(a–c) proves the steady decrease in the absorption spectra for the degradation of RhB dye with

$\text{CeO}_2/\text{La}_2\text{O}_3$  binary metal oxide nanoplates with help of photoirradiation. It is observed that the illumination of light on aqueous suspension of RhB dye in the presence of  $\text{CeO}_2/\text{La}_2\text{O}_3$  binary metal oxide nanoplates leads to diminish in absorption spectra at 554 nm. The absorbance spectra at 554 nm considerably decreases with increasing contact time (min) and gradually reduces until 210 min and the photo-degradation of RhB dye in presence of  $\text{CeO}_2/\text{La}_2\text{O}_3$  binary metal oxide nanoplates is close to 54.3%, 77% and 97% at pH 3, 7 and 9. The complete degradation of RhB dye occurs after 270 min in neutral and 330 min in acidic medium. The changes in absorption intensity vs. illumination time (min) of the synthetic RhB dye in the presence of  $\text{CeO}_2/\text{La}_2\text{O}_3$  binary metal oxide nanoplates are given in Fig. 8(d). The percentage degradation was plotted with irradiation time (min) for the oxygen saturated aqueous suspension of RhB in the presence of  $\text{CeO}_2/\text{La}_2\text{O}_3$  binary metal oxide nanoplates is shown in Fig. 8(e). Finally, the degradation of RhB evidently verified that the prepared nanomaterials acquire significant photocatalytic activity and these  $\text{CeO}_2/\text{La}_2\text{O}_3$  binary metal oxide nanoplates could be beneficial - photocatalysts for the removal of coloured dyes (Montini et al., 2016; Issarapanacheewin et al., 2016; Rahman et al., 2014; Kaviyarasua et al., 2017).

### 3.8.3. Visible light induced decomposition of Rhodamine- B using $\text{CeO}_2/\text{La}_2\text{O}_3$ heterogeneous catalyst ( $\text{Ce}_2/\text{La}_1$ )

To evaluate the photocatalytic activities of the synthesized  $\text{CeO}_2/\text{La}_2\text{O}_3$  binary metal oxide nanoplates ( $\text{Ce}_2/\text{La}_1$ ), the visible light

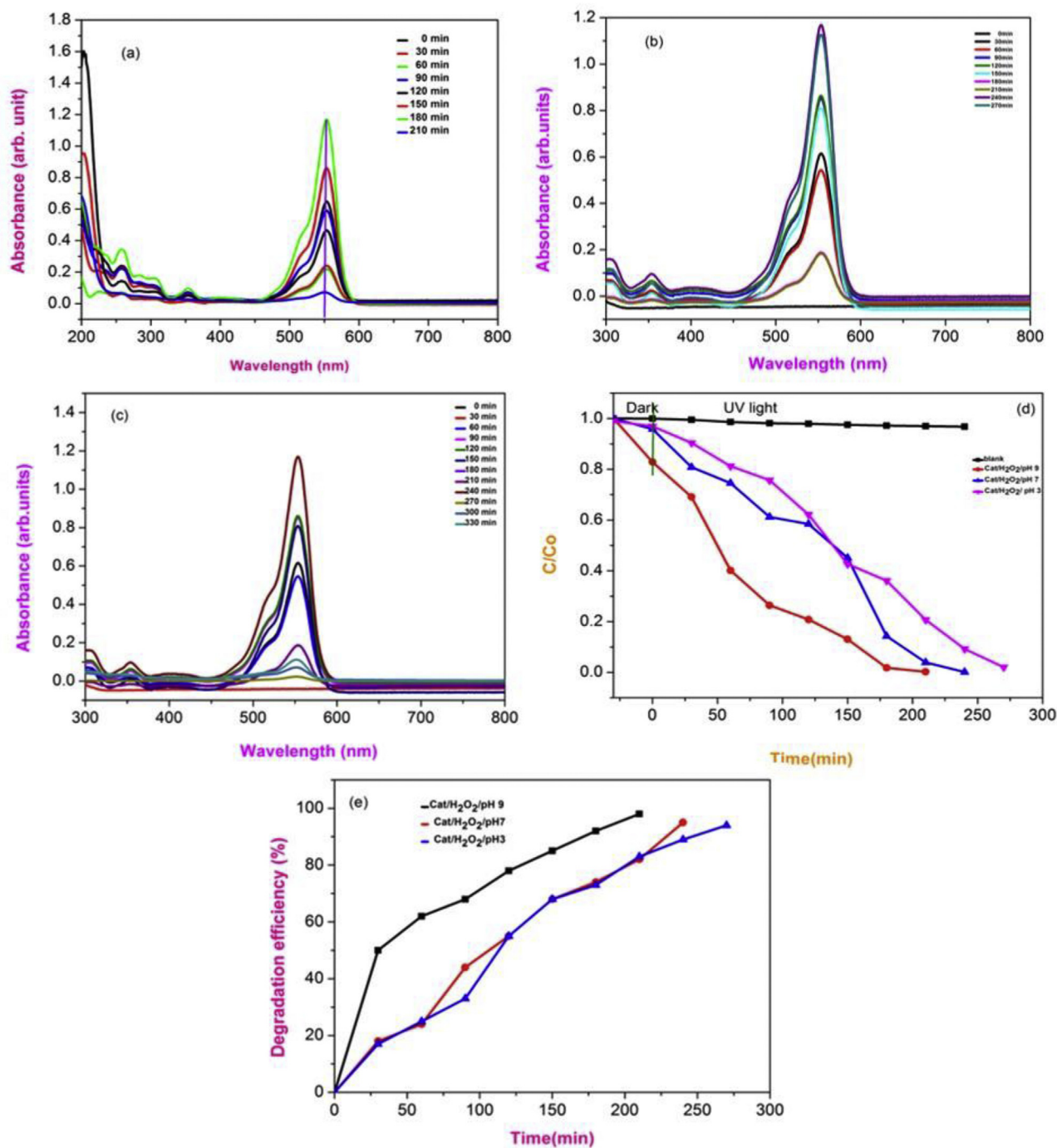


**Fig. 8.** Effect of photocatalytic degradation for RhB dye solution in the dark and under UV light irradiation at different time intervals (a) spectral changes of dye with catalyst-H<sub>2</sub>O<sub>2</sub> at pH 9.0 (b) spectral changes of dye with catalyst-H<sub>2</sub>O<sub>2</sub> at pH 7.0 (c) spectral changes of dye with catalyst-H<sub>2</sub>O<sub>2</sub> at pH 3.0 (d) C/C<sub>0</sub> vs. time (min) plot for then photodegradation/decolourization of dye and (e) percentage of efficiency, in the presence of catalyst-H<sub>2</sub>O<sub>2</sub> at pH 9.0, pH 7.0 and pH 3.0.

irradiation was used for the decomposition of well-known organic dye RhB and the absorbance spectrum of RhB synthetic dye is presented in Fig. 9. The absorption spectrum at 554 nm decreases evenly for the decomposition of RhB dye. The pink colour of the RhB dye solution becomes colourless with catalyst is confirmed from the absorption spectra which are significantly decreased at 554 nm with increase in visible light exposure time (min). The efficiency of the decomposition of dye was found to be 98%, which takes place after 120 min of irradiation of visible light in the presence of synthesized CeO<sub>2</sub>/La<sub>2</sub>O<sub>3</sub> binary metal oxide nanoplates. The changes in the absorption intensity with irradiation time (min) for the degradation of RhB in the presence of

synthesized CeO<sub>2</sub>/La<sub>2</sub>O<sub>3</sub> binary metal oxide nanoplates are shown in Fig. 9 (Gu et al., 2015; Kasinathan et al., 2016).

#### 3.8.4. Effect of pH on the photodegradation of Rhodamine-B dye

Decomposition rate of dye depends on the pH. In case of acid medium, the positive charge is formed because of the presence of hydronium ions, and this leads to reduction in the number of active sites on the surface of the heterogeneous binary metal oxide catalyst. However, the substrate adsorbed on the nanomaterials surface, which directly affects the electron transfer among the energized state organic dye effluent and heterogeneous catalyst supplementary, influences the

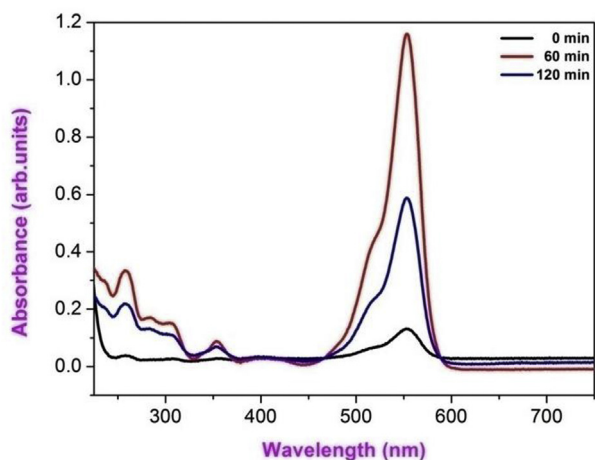


Fig. 9. Effect of photocatalytic degradation for RhB dye solution under visible light irradiation at different time intervals (catalyst- $\text{H}_2\text{O}_2$  at pH 9.0).

Table 1

List of binary metal oxides of  $\text{CeO}_2$  used for the photocatalytic degradation of organic pollutants.

T. No.	Binary oxide	Pollutants	References
1	$\text{CeO}_2/\text{ZnO}$	acridine orange and methylene blue, 4-nitrophenol, hydrogen evolution	(Faisal et al., 2013; Saravanakumar et al., 2018; Zeng et al., 2014)
2	$\text{CeO}_2/\text{CdS}$	Rhodamine-B	(Gu et al., 2015)
3	$\text{CeO}_2/\text{TiO}_2$	Rhodamine-B	(Kasinathan et al., 2016)
4	$\text{CuBi}_2\text{O}_4/\text{CeO}_2$	Congo Red	(Elaziouti et al., 2015)
5	$\text{CeO}_2/\text{TiO}_2$	Bromophenol Dye	(Ameen et al., 2014)
6	$\text{CeO}_2/\text{Co}_2\text{O}_3$	Methylene Blue	(Saranya et al., 2014)
7	$\text{MoO}_3/\text{CeO}_2$	Rhodamine-B and Safranin-T	(Zhao et al., 2010)
8	$\text{CeO}_2/\text{TiO}_2$	Methylene Blue	(Magesh et al., 2009)
9	$\text{CeO}_2/\text{La}_2\text{O}_3$	Rhodamine-B	present work

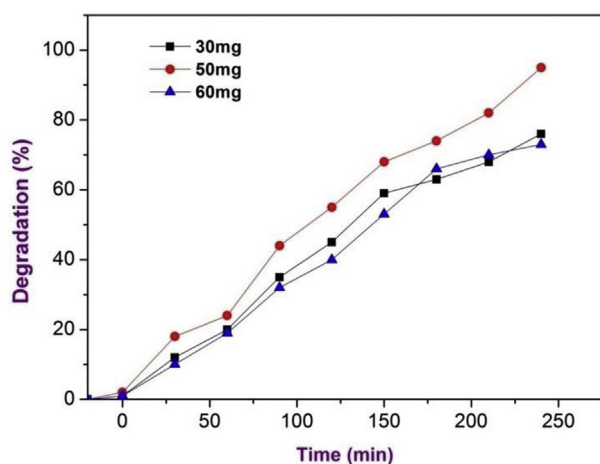


Fig. 10. Effect of catalyst dose on the photodegradation of Rhodamine-B dye.

rate of the degradation reaction. At low pH values, the semiconductor surface carries a net positive charge, which leads to poor adsorption of the dye or their intermediates on the catalyst. The rate of the reaction was found to increase with increase in pH. This in turn can lead to their efficient photocatalytic degradation. This is because of the

heterostructured binary metal oxide surfaces that were predominantly negatively charged due to the presence of hydroxyl groups at higher pH. With higher pH values, the creation of active  $\cdot\text{OH}$  species is favoured, not only to get better transfer of holes to the adsorbed hydroxyls, but also to have electrostatic attractive effects connecting the negatively charged  $\text{CeO}_2$  based heterogeneous catalyst particles and the functioning cationic dyes.

### 3.8.5. Effect of irradiation time on the photodegradation of Rhodamine-B dye

The degradation efficiency of RhB increases with an increase in the irradiation time for heterostructured  $\text{CeO}_2/\text{La}_2\text{O}_3$  binary metal oxide nanoplates. This is due to the movement of valence electron from the low energy state by absorbing higher energy photons to the excited state by the illumination of UV light, which leads to the creation of photoexcited electron in the conduction band. This photoexcited electron in the conduction band trapped by surface oxygen molecules generates highly reactive hydroxyl radicals in the system, which changes the colour of the dye. The photodegradation efficiency of nanomaterials at different time intervals was carried out to examine the effect of irradiation time on the photodegradation of RhB at room temperature. Fig. 9 shows the decomposition of RhB dye is directly proportional to UV irradiation time.

### 3.8.6. Effect of catalyst dose on the photodegradation of Rhodamine-B dye

As the catalyst loading increases, the photocatalytic degradation rate initially increases and then decreases. The maximum degradation is observed for 10 ppm RhB dye with 50 mg of the catalyst on irradiation with 365 nm light and visible light as shown in Fig. 10. With increased catalyst loading, the number of active sites in the solution will increase, but the penetration of light decreases, because of the excessive particle concentration. Moreover, at high catalyst concentration, there is a reduction in the catalyst surface area, due to the agglomeration of the particles.

### 3.8.7. Effect of initial concentration of Rhodamine-B dye

The rate of decomposition of RhB is found to increase with an increase in the initial concentration of RhB dye from 5 to 10 ppm and decreased as the concentration is increased from 15 to 20 ppm as shown in Fig. 11. At low concentrations of RhB, the number of catalytic sites will not be the preventive factor and the rate of degradation will be comparative to the RhB dye concentration. As the concentration of RhB dye increases, more and more RhB molecules are adsorbed on the surface of the photocatalyst. The reactive species ( $\cdot\text{OH}$  and  $\cdot\text{O}_2$ )

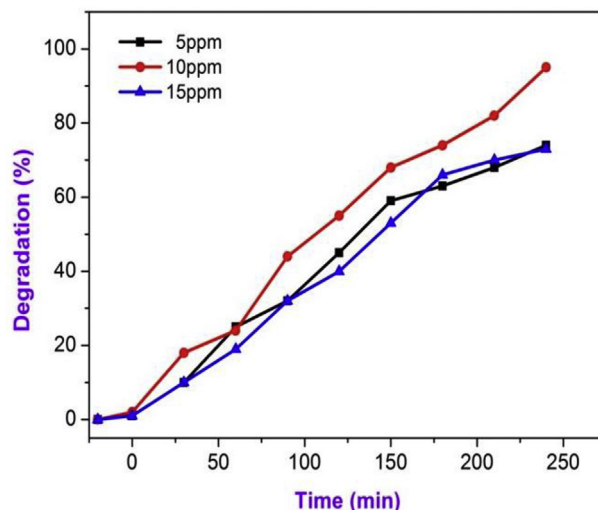


Fig. 11. Effect of initial concentration of Rhodamine-B dye.

necessary for the degradation of the organic pollutant on the catalyst surface remains constant for a given light intensity, catalyst quantity and period of the irradiation. Hence, the accessible  $\cdot\text{OH}$  radicals are insufficient for the organic effluent degradation at higher level concentrations. Thus, the dye degradation rate decreases as the concentration increases.

### 3.8.8. Effect of reusability of the catalysts on photodegradation of Rhodamine-B dye

The recyclability of the heterostructured binary metal oxide catalysts was examined by the filtration of the used  $\text{CeO}_2$  based material. It was washed with distilled water and dried at  $120^\circ\text{C}$  in an oven for 2 h and dried sample is used for the degradation process. The reused  $\text{CeO}_2$  based catalyst showed only minimum changes in the efficiency on each use. It is noteworthy that after three cycles, its degradation efficiency is reduced only by minimum percentage (2%), thus indicating that the  $\text{CeO}_2$  based heterogeneous catalyst is highly stable.

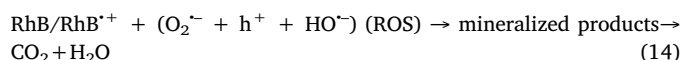
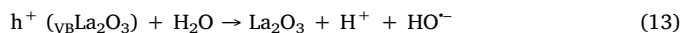
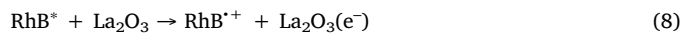
### 3.8.9. Removal of RhB from urban wastewater

The percentage of degradation of RhB in industrial wastewater is found nearly 70% for the  $\text{Ce}_2/\text{La}_1$  nanostructures. Hence, the available  $\cdot\text{OH}$  radicals are inadequate for the degradation of pollutants in the wastewater. It is because of the presence of mixture of organic compounds. Hence, the photocatalytic effect towards the industrial water is reduced than the individual dye. To illustrate the competency of our synthesized  $\text{CeO}_2/\text{La}_2\text{O}_3$  binary metal oxide nanoplates, the adequate photocatalytic effect for RhB in real wastewater was studied. The above same photocatalytic degradation experiments were carried out in industrial wastewater by using  $\text{CeO}_2/\text{La}_2\text{O}_3$  binary metal oxide nanoplates catalyst. The industrial waste water which is containing Rhodamine - B dye (100 ml) with 50 mg catalyst/ $\text{H}_2\text{O}_2$  at pH 9, was placed inside the photocatalytic reactor setup and subjected to irradiation by a UV light source ( $\lambda_{\text{max}} = 365 \text{ nm}$ ). The absorbance capacity was measured for industrial wastewater with increasing different time intervals using UV-Visible spectrophotometer. The absorption value of RhB was decreased consistently (at 552 nm), due to the structural diminishing of RhB molecules. From the plot of  $C_t/C_0$  versus irradiation time for the photocatalytic degradation of industrial wastewater, the dye degradation efficiency in wastewater was 70% for RhB dye, after 150 min of irradiation time, thus indicating the potential use of these materials in real wastewater treatment applications. Our present work proves that the increase in  $\text{La}^{3+}$  ion concentration on the crystal lattice of  $\text{CeO}_2$  leads to the reduce in crystallite grain size with increase in the active surface area, which is easily available for greater adsorption of dye molecules above the catalyst surface. Thus, the dye molecules, which are readily adsorbed in the surface of catalyst, will undergo decomposition.

### 3.8.10. Mechanism for the photodegradation of Rhodamine-B dye

The schematic representation of RhB dye degradation with binary metal oxide nanoplates is presented in Fig. 12. Mechanism of binary metal oxide photocatalysis has been discussed in literature. When a co-doped semiconductor such as  $\text{CeO}_2/\text{La}_2\text{O}_3$  binary metal oxide nanoplates absorbs a photon of energy higher than its bandgap, leads to construction of excitons (Zhao et al., 2015b). If charge partition is reserved, the negative electron and the positive hole may move to the surface of the nanoplates, which increase the redox reactions in the aqueous organic substrates in the presence of free oxygen molecule. In the photocatalytic oxidation processes hydroxyl radicals and superoxide radical anions are the major oxidizing species. Kasinathan et al., proved the photocatalytic activity 1%  $\text{CeO}_2/\text{TiO}_2$  catalyst is due to formation of hydroxyl radicals (Kasinathan et al., 2016), which is the dominant active species in the photocatalytic process. These oxidative processes would result in the mineralization of the synthetic RhB solution. Alternatively, the RhB dye absorb light directly and moves to excited state ( $\text{RhB}^*$ ), which leads to charge injection in the conduction

band of the semiconductor as given in the following equations (Tian-Yi et al., 2009; Wan-Kuen and Tayade, 2014; Kaviyarasu et al., 2017a). The photodegradation route was initiated by the photolysis of binary metal oxide nanoplates oxide/hydroxyl species.



Both the rare-earth metal ions, performing as Lewis acids, evidently show greater capability of trapping photogenerated conduction band electrons. The trapped electrons in  $\text{Ce}^{4+}/\text{Ce}^{3+}$  system was later moved to the  $\text{O}_2$  molecule present in the surface level of the catalyst. On illumination of UV or visible light, the transportation of higher energy electrons can capture various paths. The valance band electrons of  $\text{La}_2\text{O}_3$  shifted to the Ce 4f state and then the electrons credibly are moved to  $\text{Ce}^{4+}$  by the formation of  $\text{Ce}^{3+}$ :



Therewith, the trivalent ceria ( $\text{Ce}^{3+}$ ) may shift its electron to the surface active free oxygen molecules to give active oxygen radicals with electron, in such a way they get the charge variation (Kaviyarasu et al., 2016):



Afterwards, in the next footstep, the establishment of hydroxyl radicals was generated from the reaction between the oxygen radicals and positive protons in the aqueous solution;



So, from this mechanism the cerium ion transfers its electrons to free  $\text{O}_2$  and generates hydroxyl radicals on the surface of the catalyst. The positive holes in the valance band react with the hydroxyl ions in the water to form hydroxyl radicals. These hydroxyl radicals degrade the dyes to  $\text{CO}_2$  and  $\text{H}_2\text{O}$  as shown in Fig. 12, which describes the photocatalytic degradation for ceria based samples. When the amount of Ce exceeded in the samples the photocatalytic degradation for ceria based samples increases. The changes in the activity of the samples were due to the reduction in the competent separation of photo-generated electron-hole pairs on the surface of the catalysts.

## 4. Conclusion

Lanthanum decorated ceria heterostructured binary metal oxide nanoplates were synthesized by using the hydrothermal method. The physical and chemical nature of these nanoplates was studied with the help of different analytical methods. XRD dimensions support that these synthesized materials are made up of the cubic crystalline phase with high active surface area. HRTEM images of the ceria based binary metal oxides prove the formation of nanoplates with the grain size nearly 10–30 nm. Photocatalytic degradation of dye was carried out on the nanoplates surfaces. The PL spectra proved the existence of blue-emission in the visible region. In this present investigation, the dye decomposition rate is higher for 10 ppm of dye concentration, due to more active site is accessible for dyes to be adsorbed on the active surfaces of  $\text{CeO}_2$  based nanoplates at less concentration of dye. Whereas

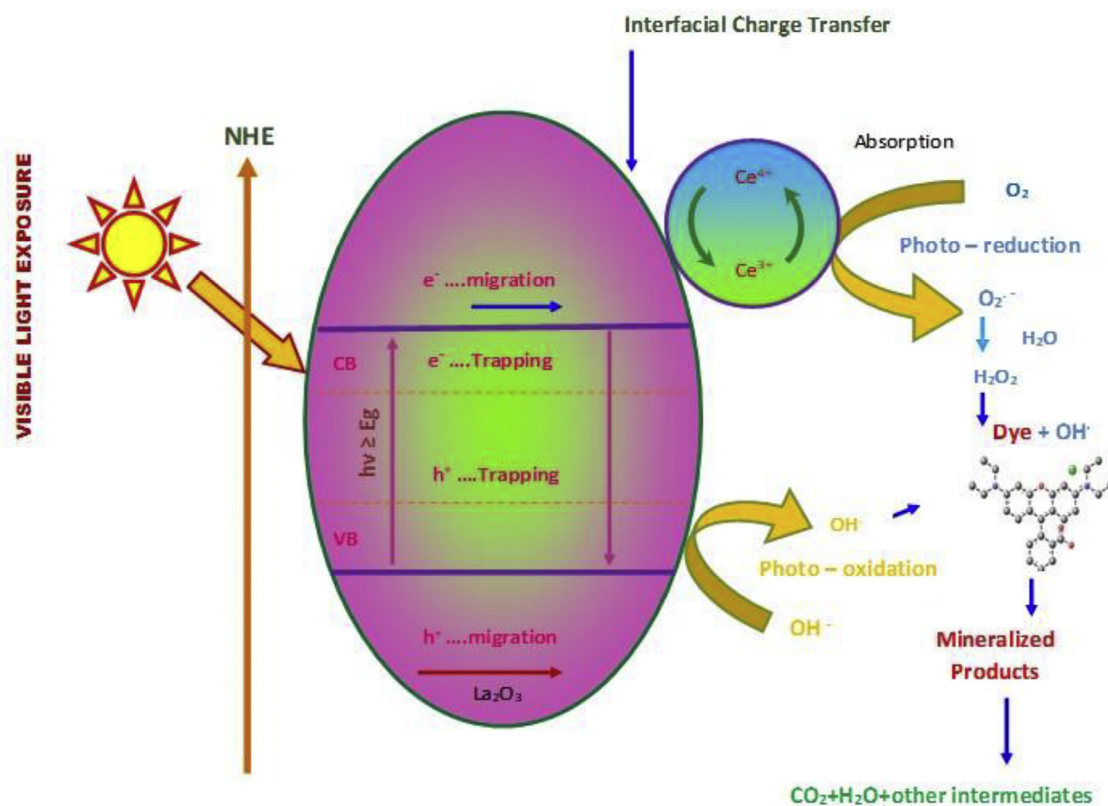


Fig. 12. Schematic diagram of the charge separation of CeO<sub>2</sub>/La<sub>2</sub>O<sub>3</sub> nanostructure showing photogenerated electron transportation processes leading to the UV light driven photocatalytic degradation of dye.

longer time is required to reach the complete degradation at higher concentrations of RhB compared to 10 ppm of RhB. The specific platelets of CeO<sub>2</sub> based nanoplates lead to larger active surface area (SA), furnish more chemically active position and raise the decomposition of the dye molecules than the pure metal oxide photocatalysts. Therefore, ultrafine CeO<sub>2</sub> based nanostructure catalysts possessed synergic effects, which will lead to the decomposition of the individual polluting organics. The Ce<sub>2</sub>/La<sub>1</sub> and Ce<sub>1</sub>/La<sub>1</sub> samples showed higher photocatalytic activity in the decomposition of industrial effluent RhB under UV and visible light irradiation. This method can be extended to the other metal oxides for opto and bio-electronic requests.

#### Conflicts of interest

This manuscript or a very similar manuscript has not been published, nor is under consideration by any other journal. All authors have seen and approved the final, submitted version of this manuscript. The authors declare no competing financial interest. There are no conflicts of interest to declare.

All authors declare that there is no conflict of interest.

#### Notes

The authors declare no competing financial interest.

#### Acknowledgement

The authors gratefully acknowledge research funding from UNESCO-UNISA Africa Chair in Nanosciences/Nanotechnology Laboratories, College of Graduate Studies, University of South Africa (UNISA), Muckleneuk Ridge, Pretoria, South Africa, (Research Grant Fellowship of framework Post-Doctoral Fellowship program under contract number Research Fund: 139000). One of the authors (Dr. K.

Kaviyarasu) is grateful to Prof. M. Maaza, Nanosciences African network (NANOAFNET), Materials Research Department (MRD), iThemba LABS-National Research Foundation (NRF), Somerset West, South Africa for his constant support, help and encouragement.

#### Appendix A. Supplementary data

Supplementary data to this article can be found online at <https://doi.org/10.1016/j.sajce.2018.09.003>.

#### References

- Ahmed, S., 2015. Influence of parameters on the heterogeneous photocatalytic degradation of pesticides and phenolic contaminants in wastewater: a short review. *J. Environ. Mang.* 12, 201103.
- Ameen, S., Shaheer Akhtar, M., Seo, H.K., Shin, H.S., 2014. Solution-processed CeO<sub>2</sub>/TiO<sub>2</sub> nanocomposite as potent visible light photocatalyst for the degradation of bromophenol dye. *Chem. Eng. J.* 247, 193–198. <https://doi.org/10.1016/j.cej.2014.02.104>. Available online.
- Bakkiyaraj, R., Bharath, G., Hasini Ramsait, K., Abdel-Wahab, A., Alsharaeh, E.H., Shen-Ming, C., Balakrishnan, M., 2016. Solution combustion synthesis and physicochemical properties of ultrafine CeO<sub>2</sub> nanoparticles and their photocatalytic activity. *RSC Adv.* 22, 567.
- Elaziouti, A., Laouedj, N., Bekka, A., Vannier, R., 2015. Preparation and characterization of p-n heterojunction CuBi<sub>2</sub>O<sub>4</sub>/CeO<sub>2</sub> and its photocatalytic activities under UVA light irradiation. *J. King Saud Univ. Sci.* 27, 120.
- Faisal, M., Ismail, A.A., Ibrahim, A.A., Bouzid, H., Al-Sayari, S.A., 2013. Highly efficient photocatalyst based on Ce doped ZnO nanorods: controllable synthesis and enhanced photocatalytic activity. *Chem. Eng. J.* 229, 225–233.
- Gu, S., Chen, Y., Yuan, X., Wang, H., Chen, X., Liu, Y., Jiang, Q., Wu, Z., Zeng, G., 2015. Facile synthesis of CeO<sub>2</sub> nanoparticles sensitized CdS nanorods photocatalyst with improved visible light photocatalytic degradation of Rhodamine-B. *RSC Adv.* 5, 79556–79564. <https://doi.org/10.1039/C5RA16114B>.
- Hemalatha, K.S., Rukmani Synthesis, K., 2016. Characterization and optical properties of polyvinyl alcohol-cerium oxide nanocomposite films. *RSC Adv.* 6, 74354.
- Issarapanacheewin, S., Wetchakun, K., Phanichphant, S., Kangwansupamonkon, W., Wetchakun, N., 2016. Efficient photocatalytic degradation of Rhodamine B by a novel CeO<sub>2</sub>/Bi<sub>2</sub>WO<sub>6</sub> composite film. *Catal. Today* 278, 280–290. Available online. <https://doi.org/10.1016/j.cattod.2015.12.028.12.028>.

- Jaoude, M., Polychronopoulou, K., Hinder, S.J., Katsiotis, M.S., Baker, M.A., Greish, Y.E., Alhassan, S.M., 2016. Synthesis and properties of 1D Sm-doped CeO<sub>2</sub> composite nanofibers fabricated using a coupled electrospinning and sol-gel methodology. *Ceram. Int.* 45, 456.
- Kasinathan, K., Kennedy, J., Manikandan, E., Henini, M., Maaza, M., 2016. Photodegradation of organic pollutants RhB dye using UV simulated sunlight on ceria based TiO<sub>2</sub> nanomaterials for antibacterial applications. *Sci. Rep.* 6, 38064.
- Kaviyarasu, K., Fuku, X., Mola, G.T., Manikandan, E., Kennedy, J., Maaza, M., 2016. Photoluminescence of well-aligned ZnO doped CeO<sub>2</sub> nanoplatelets by a solvothermal route. *Mater. Lett.* 183, 351–354.
- Kaviyarasu, K., Geetha, N., Kanimozhi, K., Maria Magdalane, C., Sivaranjani, S., Ayeshamariam, A., Kennedy, J., Maaza, M., 2017a. In vitro cytotoxicity effect and antibacterial performance of human lung epithelial cells A549 activity of Zinc oxide doped TiO<sub>2</sub> nanocrystals: investigation of bio-medical application by chemical method. *Mater. Sci. Eng. C* 74, 325–333.
- Kaviyarasu, K., Murmu, P.P., Kennedy, J., Thema, F.T., Douglas, Letsholathebe, Kotsedi, L., Maaza, M., 2017b. Structural, optical and magnetic investigation of Gd implanted CeO<sub>2</sub> nanocrystals. *Nucl. Instrum. Methods Phys. Res. Sect. B Beam Interact. Mater. Atoms* 409, 147–152.
- Kaviyarasu, K., Magdalane, C.M., Kanimozhi, K., Kennedy, J., Siddhardha, B., Subba Reddy, E., Kumar Rotte, N., Sharma, C.S., Thema, F.T., Letsholathebe, D., Mola, G.T., Maaza, M., 2017. Elucidation of photocatalysis, photoluminescence and antibacterial studies of ZnO thin films by spin coating method. *J. Photochem. Photobiol. B Biol.* 173, 466–475.
- Kennedy, J., Leveneur, J., Williams, G.V.M., Mitchell, D.R.G., Markwitz, A., 2011. Fabrication of surface magnetic nanoclusters using low energy ion implantation and electron beam annealing. *Nanotechnology* 22, 115602.
- Korake, P.V., Dhabbe, R.S., Kadam, A.N., Gaikwad, Y.B., Garadkar, K.M., 2014. Highly active lanthanum doped ZnO nanorods for photodegradation of metasytox. *J. Photochem. Photobiol. B Biol.* 130, 11–19.
- lavkova, J., Khalahan, I., Chundak, M., Vorokhta, M., Potin, V., Matolin, V., Matolinova, I., 2015. Growth and composition of nanostructured and nanoporous cerium oxide thin films on graphite foil. *Nanoscale*. <https://doi.org/10.1039/c0xx00000x>. Available online.
- Lin, K., Chowdhury, S., 2010. Synthesis, characterization, and application of 1-D cerium oxide nanomaterials: a review. *Int. J. Mol. Sci.* 11, 3226–3251.
- Lv, Z., Zhong, Q., Ou, M., 2016. Utilizing peroxide as precursor for the synthesis of CeO<sub>2</sub>/ZnO composite oxide with enhanced photocatalytic activity. *Appl. Surf. Sci.* 376, 91–96.
- Magesh, G., Viswanathan, B., Viswanathan, R.P., Varadarajan, T.K., 2009. Photocatalytic behaviour of CeO<sub>2</sub>-TiO<sub>2</sub> system for the degradation of methylene blue. *Indian J. Chem.* 48A, 480.
- Montini, T., Melchionna, M., Monai, M., Fornasiero, P., 2016. Fundamentals and catalytic applications of CeO<sub>2</sub>-based materials. *Chem. Rev.* 116, 5987.
- Muduli, S.K., Wang, S., Chen, S., Fan Ng, C., Huan, C.H.A., Sum, T.C., Soomm, H.S., 2014. Mesoporous cerium oxide nanospheres for the visible-light driven photocatalytic degradation of dyes. *Beilstein J. Nanotechnol.* 5, 517–523.
- Nasir, M., Bagwasi, S., Jiao, Y., Chen, F., Tian, B., Zhang, J., 2014. Characterization and activity of the Ce and N co-doped TiO<sub>2</sub> prepared through hydrothermal method. *Chem. Eng. J.* 236, 388–397.
- Rahman, M.M., Bahadar Khan, S., Marwani, H.M., Asiri, A.M., Alamry, K.A., Abdul Rub, M., Khan, A., Parwaz Khan, A.A., Azum, N., 2014. Facile synthesis of doped ZnO-CdO nanoblocks as solid-phase adsorbent and efficient solar photo-catalyst applications. *J. Ind. Eng. Chem.* 20, 1071.
- Saranya, J., Ranjith, K.S., Saravanan, P., Mangalaraj, D., Rajendra Kumar, R.T., 2014. Cobalt-doped cerium oxide nanoparticles: enhanced photocatalytic activity under UV and visible light irradiation. *Mater. Sci. Semicond. Process.* 26, 218–224.
- Saravanakumar, D., Sivaranjani, S., Kaviyarasu, K., Ayeshamariam, A., Ravikumar, B., Pandiarajan, S., Veeralakshmi, C., Jayachandran, M., Maaza, M., 2018. *J. Semiconduct.* 39 (3), 033001.
- Srinivasan, R., Rajeswari Yogamalar, N., Elanchezhian, J., Justin Joseyphus, R., Chandrasekhar Bose, A., 2010. Structural and optical properties of europium doped yttrium oxide nanoparticles for phosphor applications. *J. Alloy. Comp.* 496, 472–477.
- Tian-Yi, M., Jian-Liang, C., Gao-Song, S., Xue-Jun, Z., Zhong-Yong, Y., 2009. Hierarchically structured squama-like cerium-doped titania: synthesis, photoactivity, and catalytic CO oxidation. *J. Phys. Chem. C* 113, 16658–16667.
- Wan-Kuen, J., Tayade, R.J., 2014. Recent developments in photocatalytic dye degradation upon irradiation with energy-efficient light emitting diodes. *Chin. J. Catal.* 35, 1781–1792.
- Yin, X., Zhang, Y., Fang, Z., Xu, Z., Zhu, W., 2012. Hydrothermal synthesis of CeO<sub>2</sub> nanorods using a strong base-weak acid salt as the precipitant. *Nanosci. Methods* 1 (1), 115–122.
- Zeng, C., Xie, S., Yu, M., Yang, Y., Lu, X., Tong, Y., 2014. Facile synthesis of large-area CeO<sub>2</sub>/ZnO nanotube arrays for enhanced photocatalytic hydrogen evolution. *J. Pow. Sou.* 247, 545.
- Zhang, C., Zhang, X., Wang, Y., Xie, S., Liu, Y., Lu, X., Tong, Y., 2014. Facile electrochemical synthesis of CeO<sub>2</sub> hierarchical nanorods and nanowire with excellent photocatalytic activities. *New J. Chem.* 38, 2581.
- Zhao, J., Wu, T., Wu, K., Oikawa, K., Hidaka, H., Serpone, N., 1998. Photo assisted degradation of dye pollutants. Degradation of the cationic dye rhodamine B in aqueous anionic surfactant/TiO<sub>2</sub> dispersions under visible light irradiation: evidence for the need of substrate adsorption on TiO<sub>2</sub> particles. *Environ. Sci. Technol.* 32, 2394–2400.
- Zhao, S., Li, J., Wang, L., Wang, X., 2010. Degradation of rhodamine B and Safranin-T by MoO<sub>3</sub>:CeO<sub>2</sub> nanofibers and air using a continuous mode. *Clean-Soil. Air, Water* 38 (3), 268.
- Zhao, M., Li, H., Shen, X.P., Ji, Z.Y., Xu, K.Q., 2015a. Facile electrochemical synthesis of CeO<sub>2</sub>@Ag/CdS nanotube arrays with enhanced photoelectrochemical water splitting performance. *Dalton Trans.* <https://doi.org/10.1039/C5DT03661E>. Available online.
- Zhao, M., Li, H., Shen, X.P., Ji, Z.Y., Xu, K.Q., 2015b. Facile electrochemical synthesis of CeO<sub>2</sub>@Ag/CdS nanotube arrays with enhanced photoelectrochemical water splitting performance. *Dalton Trans.* <https://doi.org/10.1039/C5DT03661E>. Available online.
- Zhu, J., Zhu, Z., Zhang, H., Lu, H., Qiu, Y., Zhu, L., Küppers, S., 2016. Enhanced photocatalytic activity of Ce-doped Zn-Al multi-metal oxide composites derived from layered double hydroxide precursors. *J. Colloid Interface Sci.* 481, 144–157.